

Characterization and quantification of structure and flow in multichannel polymer membranes by MRI

S. Schuhmann^a, J.W. Simkins^b, N. Schork^a, S.L. Codd^b, J.D. Seymour^b, M. Heijnen^c, F. Saravia^a, H. Horn^a, H. Nirschl^a, G. Guthausen^{a,*}

^a Karlsruhe Institute of Technology (KIT), Institute of Mechanical Process Engineering and Mechanics and Engler Bunte Institute, Chair of Water Chemistry and Water Technology, 76131 Karlsruhe, Germany

^b Montana State University (MSU), Chemical & Biological Engineering Department and Mechanical & Industrial Engineering Department, 59717 Bozeman, MT, USA

^c Inge GmbH, Flurstrasse 27, 86926 Greifenberg, Germany

A B S T R A C T

Keywords:

MRI
Flow
Filtration
Multichannel membrane
Fouling
Sodium alginate

Polymeric multichannel hollow fiber membranes were developed to reduce fiber breakage and to increase the volume-to-membrane-surface ratio and consequently the efficiency of filtration processes. These membranes are commonly used in ultrafiltration and are operated in in-out dead-end mode. However, some of the filtration details are unknown. The filtration efficiency and flow in the multichannel membranes depend on filtration time and are expected to vary along spatial coordinates. In the current work, *in-situ* magnetic resonance imaging was used to answer these questions. Velocities were quantified in the feed channels to obtain a detailed understanding of the filtration process. Flow and deposits were measured in each of the seven channels during filtration of sodium alginate, which is a model substance for extracellular polymeric substances occurring in water treatment. Volume flow and flow profiles were calculated from phase contrast flow images. The flow in z -direction in the center channel was higher than in the surrounding channels. Flow profiles vary depending on the concentration of Ca^{2+} , which changes the filtration mechanism of aqueous solutions of sodium alginate from concentration polarization to gel layer filtration.

1. Introduction

Polymeric multichannel hollow fiber membranes are used in a wide range of water filtration applications, including waste water, drinking and sea water, surface water, pool water and others [1]. During the filtration process, deposits develop, which cause an increase in filtration resistance. These fouling processes can be controlled by means of backwashes and chemically enhanced backwashes, however modest flux levels have to be chosen in order to guarantee a good long term performance [2]. Multichannel membranes were designed to prevent fiber breakages and to increase the efficiency resulting from the higher volume to membrane surface ratio due to the larger capillary size compared to other hollow fiber membranes [3,4]. An unanswered question concerns the flow properties and deposit formation during filtration. For example, how does flow velocity distribution vary over the channels of multichannel fiber membranes during filtration processes? To address this, spatially and time resolved measurements inside of the opaque fibers are required.

MRI is an *in situ* and non invasive analytical tool which is capable to

characterize filtration processes [5–16]. Contrary to optical methods, it is possible with MRI to observe in out filtration spatiotemporally resolved. The data can be quantitatively analyzed for example in hollow fiber membranes [17–20]. Furthermore velocity images can be measured, thus flow can be analyzed spatially resolved as a function of filtration time. Not only can velocity be measured along the long axis of the cylindrical membranes, but also in the transverse plane essential for filtration. Sodium alginate was used as a model substance for extracellular polymer substances (EPS) which play a major role during biofouling [21,22]. Filtration mechanisms are affected by the concentration of divalent ions like Ca^{2+} . It is well known that sodium alginate forms gels when divalent ions are present in the aqueous solution [23], whereas pure sodium alginate in deionized water can be regarded as a macromolecular solution at concentrations $c_{\text{Ca}^{2+}} \rightarrow 0$.

In this work, MRI was used to investigate a polymeric multichannel membrane with the aim of a microscopic understanding of the filtration process in such geometries. Both, relaxation weighted intensity images and velocity images were acquired to analyze deposits and flow during filtration in each of the channels. In terms of deposit formation,

* Corresponding author.

E-mail address: gisela.guthausen@kit.edu (G. Guthausen).

Symbols			
c_{alginate}	concentration of alginate [mg/L]	\dot{V}_{total}	sum of all channel volume flows [ml/min]
$c_{\text{Ca}^{2+}}$	concentration of Ca^{2+} [mmol/L]	v_{enc}	encoded velocity [cm/s]
c_{MagAlg90}	concentration of magnetite alginate contrast agent [mmol/L]	v_x	velocity in x direction [cm/s]
M_1	first moment [$\text{T s}^2/\text{m}$]	v_y	velocity in y direction [cm/s]
RF	RARE factor []	v_z	velocity in z direction [cm/s]
rf	radio frequency [MHz]	<i>Greek letters</i>	
T_1	spin lattice relaxation time [s]	γ	gyromagnetic ratio [rad/(s T)]
T_2	transverse relaxation time [s]	Δx	in plane resolution in x direction [μm]
T_R	repetition time [s]	Δy	in plane resolution in y direction [μm]
t	filtration time [min]	τ_E	echo time [ms]
\dot{V}	volume flow [ml/min]	$\tau_{E,\text{eff}}$	effective echo time [ms]
$\dot{V}_{\text{Capillary}}$	volume flow in a channel [ml/min]	Φ	phase angle in a voxel [rad]

concentration polarization and gel layer formation can be observed also in the multichannel membranes. Differences in volume flow and flow profiles in each channel were characterized during filtration. Thereby it was possible to monitor filtration efficiency in the different channels.

2. Experimental

2.1. Model solutions for ultrafiltration: sodium alginate

Sodium alginate (“medium viscosity”, Sigma Aldrich) was used. The aqueous sodium alginate solution was obtained by stirring the alginate powder in water for 2 h at room temperature. The solution had a concentration of $c_{\text{alginate}} = 200 \text{ mg/L}$. The characteristics of the aqueous sodium alginate solution can be controlled by the concentration of divalent cations like Ca^{2+} : Alginate molecules form gels at $c_{\text{Ca}^{2+}} > 0$, while the macromolecules hardly interact in the absence of divalent ions. A common description is the egg box model, for example Ref. [24]. For this study CaCl_2 was added for the filtration of sodium alginate *with* Ca^{2+} with a concentration of $c_{\text{Ca}^{2+}} = 2 \text{ mmol/L}$ after the sodium alginate was completely dissolved.

The image contrast in MRI depends on the longitudinal relaxation T_1 and the transverse relaxation T_2 . These NMR parameters are specific of the sample. The repetition time T_R is used for designing T_1 weighting images, the echo time τ_E is the parameter which determines T_2 weighting. Since the native MRI contrast between deposit and feed solution is not sufficient, the contrast agent magnetite alginate with a mean particle size of around 90 nm (MagAlg90) was used for the in intensity images during the filtration [20]. It is a dominantly T_2 contrast agent, therefore it reduced intensities in the images, dependent on the concentration. MagAlg90 was added to the feed with a concentration of $c_{\text{MagAlg90}} = 1 \text{ mmol/L}$.

Contrast agents cannot only be used to get higher contrast between materials, they are often applied to reduce the scan time. For fast measurements of the structure of the polymeric membrane the predominantly T_1 contrast agent Gadopentetic acid (Gd DTPA) was used which is one of the most commonly applied T_1 contrast agents in clinical MRI [25]. By adding Gd DTPA the spin lattice relaxation time decreases, allowing faster scan times due to shorter the repetition time T_R . The concentration for the experiments with Gd DTPA was $c_{\text{Gd DTPA}} = 1 \text{ mmol/L}$.

2.2. Hollow fiber membrane

In the present study an “Inge Multibore® Membrane 0.9” was investigated, which has 7 channels and an average pore size of 20 nm (Fig. 1) [1]. The supporting material of the membrane is polyethersulfone (PES). The membranes are typically used in in out filtrations in dead end mode [26]. The structure of the polymeric membrane

was mapped by μ computer tomography (μCT , Fig. 1a). Density differences determine the image contrast in μCT apart from differences in the nuclear order number. In Fig. 1a, the seven channels for in out filtration can clearly be distinguished from the supporting material. The supporting material itself is structured, with dense areas representing the active membrane layer of filtration near the channels. Less dense areas are responsible for the form stability of the membrane. They are designed so that the filtration resistance is kept low and flow through the membrane from the channel to the permeate is not significantly hindered. Six areas of especially low density, i.e. large porosity, are found between the filtration channels.

The multichannel membrane is mounted into an acrylic glass module (Fig. 1b). Due to the polymeric membrane's flexibility, it is nearly impossible to center the membrane over the entire module without spacers (schematically shown in (Fig. 1b)). Therefore the membrane appears at different positions in the axial slices of the MRI images. The location of the membrane in the module might influence the velocity field, which must be considered in the interpretation of the velocity images.

2.3. In situ filtration experiments

Experiments were performed at Montana State University (MSU) with a Bruker Avance III 250 MHz tomograph and at Karlsruhe Institute of Technology (KIT) with a Bruker Avance III 200 MHz tomograph. Both use an actively shielded micro2.5 gradient and corresponding

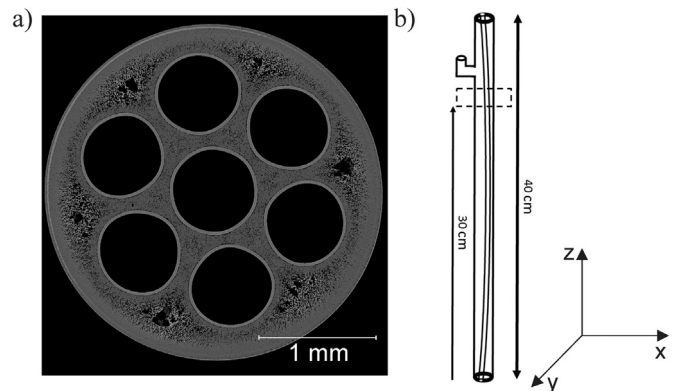


Fig. 1. (a) Structural image of a polymeric multichannel membrane by μCT with a spatial resolution of $3.94 \mu\text{m}$. The polymer density varies in the supporting material, with large pores visible in the areas between the channels. (b) Scheme of the filtration module and the field of view of MRI (dashed area). The flexible membrane is not perfectly located in the module's center over the entire module length. Axial images were measured 30 cm above the module entry, shortly before the permeate outlet.

radio frequency (rf) probes. The module was placed into the rf probe inside the magnet during filtration. A pressure vessel was connected to a 4 mm ID tube with a length of 1.50 m to ensure a fully developed flow at the module's inlet and constant pressure during filtration. A schematic drawing of the filtration setup can be found in previous work [17]. Axial flow encoded images allowed to characterize flow in the diverse channels as a function of filtration time. The images were processed within self written MATLAB scripts to calculate the volume flow and the flow profiles in the seven channels at the position near the permeate outlet shown in (Fig. 1b).

2.4. MRI methods

2.4.1. Structural characterization by RARE MRI

The rapid acquisition with relaxation enhancement (RARE) pulse sequence was used to measure the structural images of the polymeric multichannel membrane also during filtration. The method allows the characterization of the development of the fouling layer during filtration processes. This fast spin echo method acquires multiple echoes within one repetition time T_R . The number of echoes measured during T_R is denoted the RARE factor (RF). Between the π refocusing pulses the phase gradient G_{phase} of duration δ_p is set to different values, which allows the sampling of k space RF times faster than a classic spin echo imaging sequence. RARE is not as susceptible to susceptibility artefacts as a gradient echo method. Structural images can be acquired with relatively high spatial resolution without suffering too much from susceptibility differences between air, water, and PES. The contrast in a MR image can be changed by the echo time, exploring the transverse relaxation contrast as well as by the repetition time. Depending on the sorting of the echoes in k space, the effective echo time varies intrinsically in the RARE pulse sequence. The effective echo time, $\tau_{E,\text{ieff}}$, is defined as the time between the initial excitation and the collection of the zero phase echo [27]. We used two different encoding orders in our experiments:

Linear encoding: the first echo was set to the minimum of the phase encoded direction in k space and linearly decreased towards the maximum. In this case $\tau_{E,\text{ieff}}$ can be calculated by:

$$\tau_{E,\text{ieff}} = \frac{RF\tau_E}{2} \quad (1)$$

This encoding order is not as sensitive to phase artefacts, but has higher $\tau_{E,\text{ieff}}$ than the centric encoding order.

Centric Encoding: the first echo is set to the center of k space. The

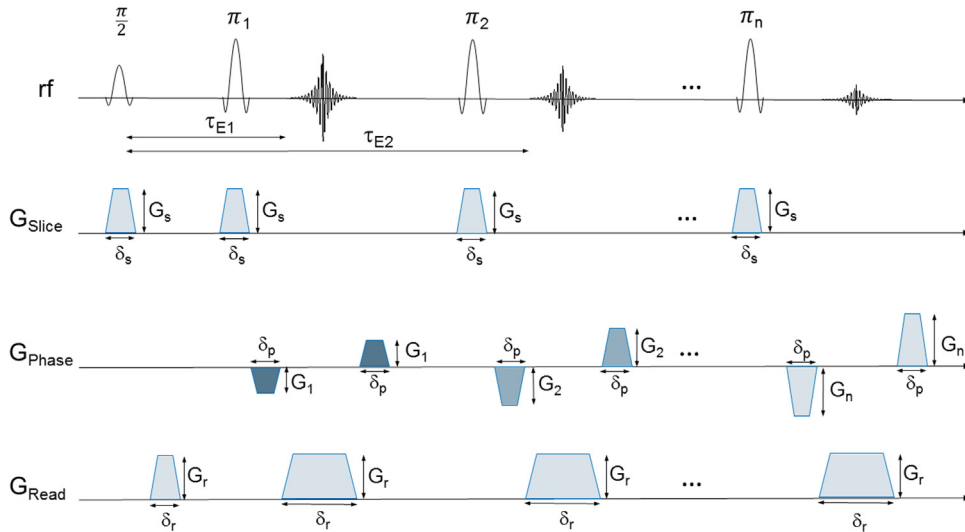


Fig. 2. RARE pulse sequence for fast spin echo imaging. During one repetition time T_R RF echoes are measured at diverse points in k -space [28]. The spatial resolution is due to the time dependent (δ) gradients G in the three dimensions.

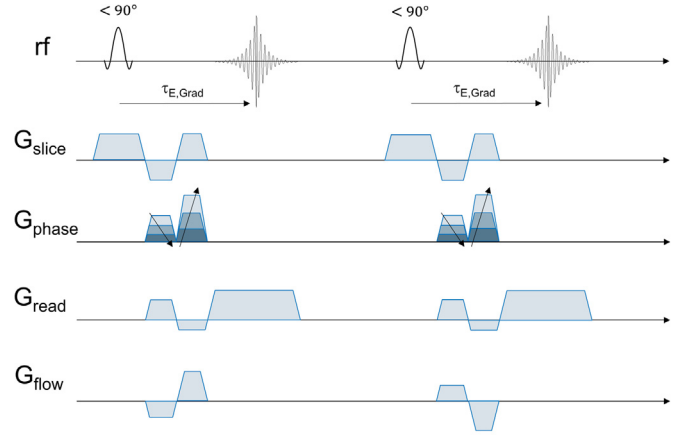


Fig. 3. Pulse sequence for measuring velocities spatially resolved (flow-map). In a slice defined by G_{slice} including flow compensation, the magnetization is spatially encoded but flow compensated by G_{phase} and G_{read} . G_{flow} encodes the component of velocity specified by the spatial direction of G_{flow} .

following echoes are set towards the extremes of k space. This results in $\tau_{E,\text{ieff}} = \tau_E$ and thereby smaller effective echo times, but this ordering is more sensitive to phase artefacts.

2.4.2. Velocity measurements by flow encoding imaging

Velocities were measured spatially and time resolved *in situ* and non invasively by MRI during filtration. A gradient echo based velocity encoding pulse sequence (flow map) was used (Fig. 2). In addition to the spatial encoding of a slice by phase and read gradients, an additional gradient pair with amplitude G_{flow} was applied, which encodes the velocity. The spatial direction of all gradients can be chosen in the experiments (Fig. 3).

We used a gradient echo pulse sequence with an excitation pulse of 90° . Two images were acquired with different flow encoding gradients. The velocity was calculated via the phase difference $\Delta\Phi$ of both images in each voxel (Eq. (1)).

$$\Delta\Phi = \Phi^{(1)} - \Phi^{(2)} = \gamma \Delta M_1 v \quad (2)$$

ΔM_1 denotes the difference of the first temporal gradient moment. Eq. (1) can be resolved with respect to velocity $v(x, y)$, where $\pi/\gamma\Delta M_1$ is abbreviated as critical velocity v_{enc} or the field of flow (FOF).

$$v(x, y) = \frac{\Delta\Phi(x, y)}{\gamma\Delta M_1} = \frac{\Delta\Phi(x, y)}{\pi} \frac{v_{enc}}{\pi} \quad (3)$$

The FOF has to be specified before the measurements in analogy to the field of view in structural imaging. If the value of FOF is too small, velocity aliasing occurs. On the other hand, if the FOF is too large it will lead to an inadequate flow resolution. During filtration the velocities in z direction dramatically decrease which requires the FOF to be adjusted from time to time during the filtration progress. Since the filtration process is relatively fast, short measurement times are necessary for an adequate time resolution. Short repetition times were used for the filtration velocity images, which leads to T_1 saturation in the image. Detailed descriptions of MRI are provided in several textbooks [29–31].

3. Results and discussion

3.1. Structural MR images of polymeric multichannel membranes

To image the structure of the multichannel hollow fiber membrane, it was mounted into a module and was surrounded by water. A wash bottle allowed the adjustment of water in the permeate. At that point, water was in the permeate but not in the channels of the membrane. A RARE image revealed the structure of the membrane exploring the relaxation contrast between polymer, air and water (Fig. 4a). The regions with low intensities indicate air. The regions with high intensities are attributed to a combination of water and the membrane polymer due to the chosen relaxation weighting. Air is observed not only in the channels but also the regions of low polymer density in the supporting material of the membrane. These inner pores were also detected in the μ CT image (Fig. 1a) Additionally, MRI allows for *in situ* detection of changes in the pores during filtration: In a second experiment the module was connected to the filtration set up and MR images were acquired while water with Gd DTPA as feed was flowing through the membrane (Fig. 4b and c). The flow channels are now filled with feed, and the amount of air in the pores decreased due to water penetration into the membrane's pores. After leaving the module one day in the tomograph and repeating the experiment, the pores filled completely with water, leaving no air in the membrane (Fig. 4c). Thus the membrane's pores were not only filled with water via convective water transport, they were also saturated via diffusion when the membrane stayed one day in the feed solution.

3.2. Structural MR images during filtration of sodium alginate

Structural images were measured during filtration of the aqueous solution of sodium alginate to characterize the deposit in the seven

channels of the membrane. The filtration was performed *without* Ca^{2+} and *with* Ca^{2+} at a constant pressure of 1 bar. The RARE pulse sequence allows relatively fast measurements (2 min 8 s) with an in plane resolution of 29.30 μm . A sufficient contrast between feed solution and fouling layer was achieved by the contrast agent MagAlg90. The development of deposits was monitored during filtration (Fig. 5). The feed solution appears in the relaxation weighted images with high intensities and the membrane with lower intensities. Deposits become larger during filtration indicated by low intensities near the membrane's inner surfaces.

A concentration polarization layer developed during the filtration *without* Ca^{2+} (Fig. 5a, b and c) as was observed in ceramic hollow fiber membranes [18]. For a sufficient temporal resolution of the intensity images during filtration, the repetition time was kept as short as possible. For this reason, inflow artifacts occur in the images. The signal intensities are therefore lower at the module's inner wall, i.e. in the permeate volume which is not quantified in the following. At the beginning of the filtration the lumen showed high intensities. With filtration time, the inner membrane surfaces get fouled by the feed containing the contrast agent MagAlg90 which leads to lower intensities due to negative paramagnetic relaxation enhancement. At the end of the filtration the deposit covers almost the complete channel area. A difference between the channels can be observed: The outer channels seem to foul faster than the channel in the center. This could be explained by the fact that the outer channels experience a lower mass transfer resistance compared to the center channel due to the smaller path length towards the permeate. The filtration rate of the outer channels may therefore be slightly larger than that of the center channel which would result in a faster growing concentration polarization layer. This phenomenon is likely to have occurred due to the high feed pressure of 1 bar, which leads to high initial flux.

During the filtration of alginate solutions, both with and without Ca^{2+} , the imaging position did not change. A change of the position was only observed after backwashing, due to the flexibility of the polymeric membrane and the increased pressure applied. A different fouling mechanism was observed for the filtration *with* Ca^{2+} . Sodium alginate forms a gel on the channel wall, which changes filtration processes from concentration polarization to gel layer formation (Fig. 5d–f). At the beginning of the filtration, the channel lumina appear with high intensities. During the filtration, a thin layer builds up at the channels inner surface. These thin gel layers appear with lower intensities again due to contrast agent MagAlg90 in the feed solution. No significant differences between channels at different spatial locations were observed in the filtration *with* Ca^{2+} .

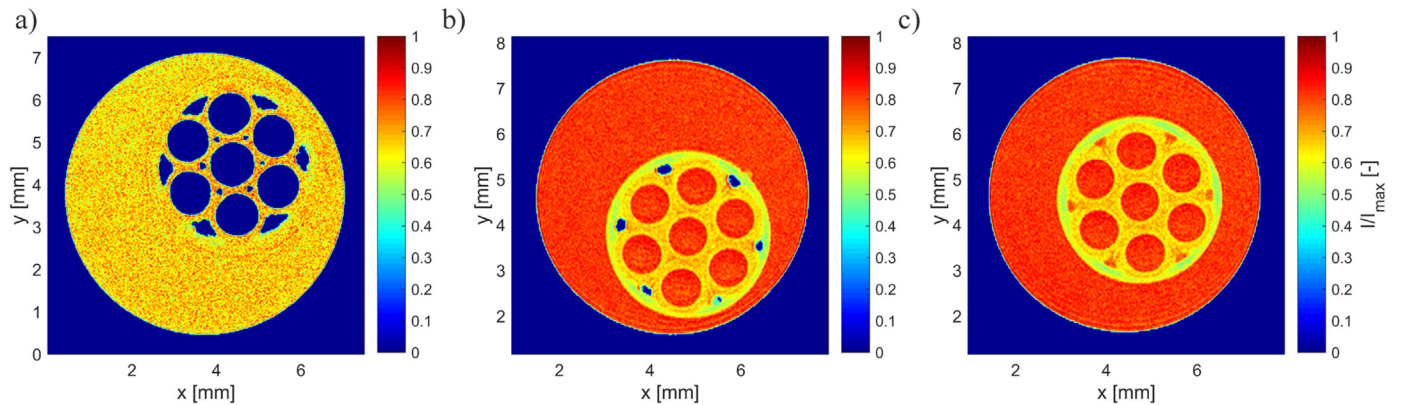


Fig. 4. (a) MRI axial image of a native multichannel membrane in a water containing module. Corresponding to the chosen relaxation weighting, polymer and water deliver roughly the same intensity. (b) During filtration with Gd-DTPA the channels were filled with water (red), air is still detected in the larger pores of the supporting material of the membrane (blue). (c) Leaving the membrane one day in the feed solution, also the large pores were filled with water, and no detectable air was left in the membrane. (For interpretation of the references to color in this figure legend, the reader is referred to the web version of this article).

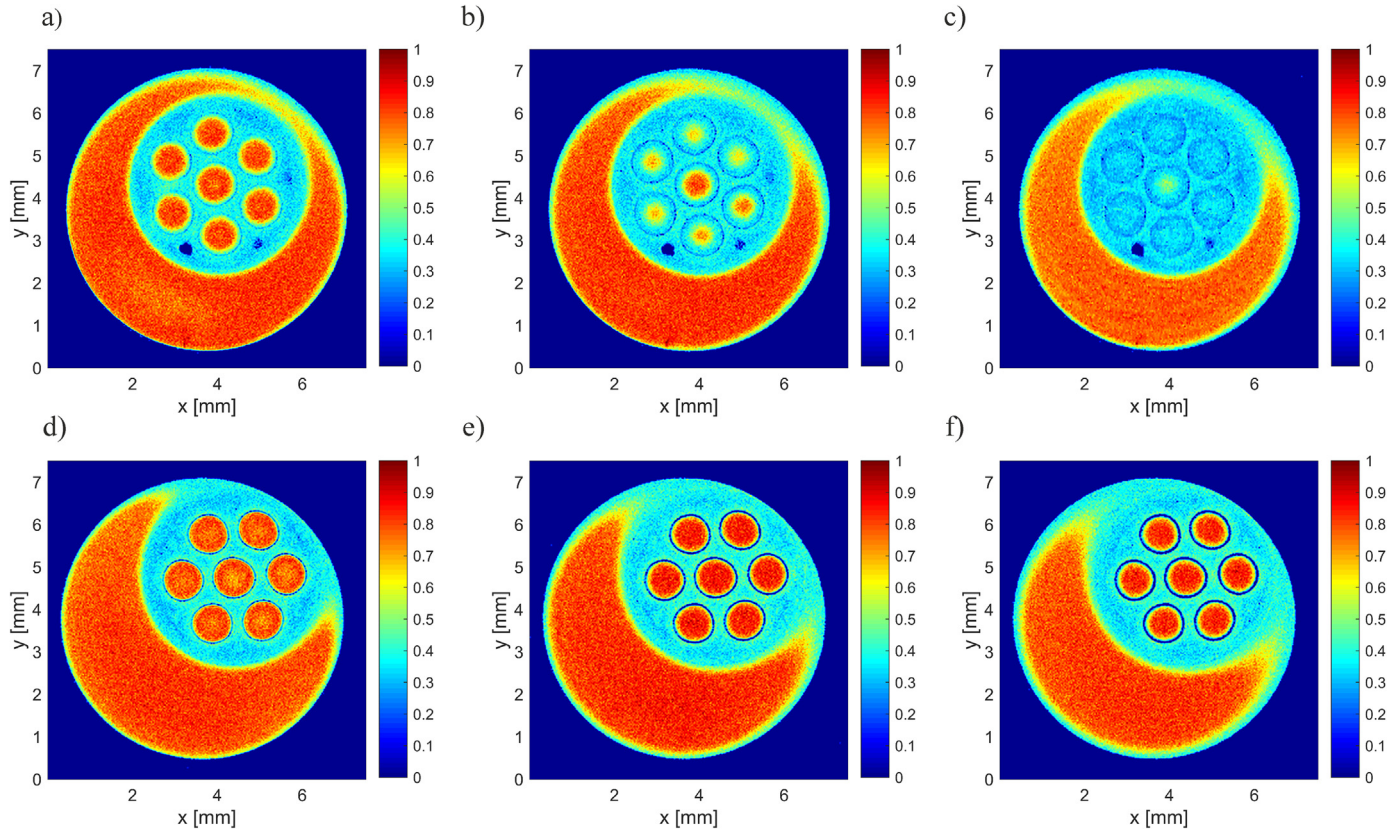


Fig. 5. T_1 and T_2 relaxation weighted MR images during filtration of an aqueous solution of sodium alginate ($c_{\text{alginate}} = 200$ mg/L) *without* Ca^{2+} (a) after 2 min 25 s, (b) after 29 min 26 s, (c) after 43 min 35 s filtration time. *With* Ca^{2+} ($c_{\text{Ca}^{2+}} = 2$ mmol/L) (d) after 4 min 44 s, (e) after 24 min 45 s, and (f) after 51 min 39 s filtration time.

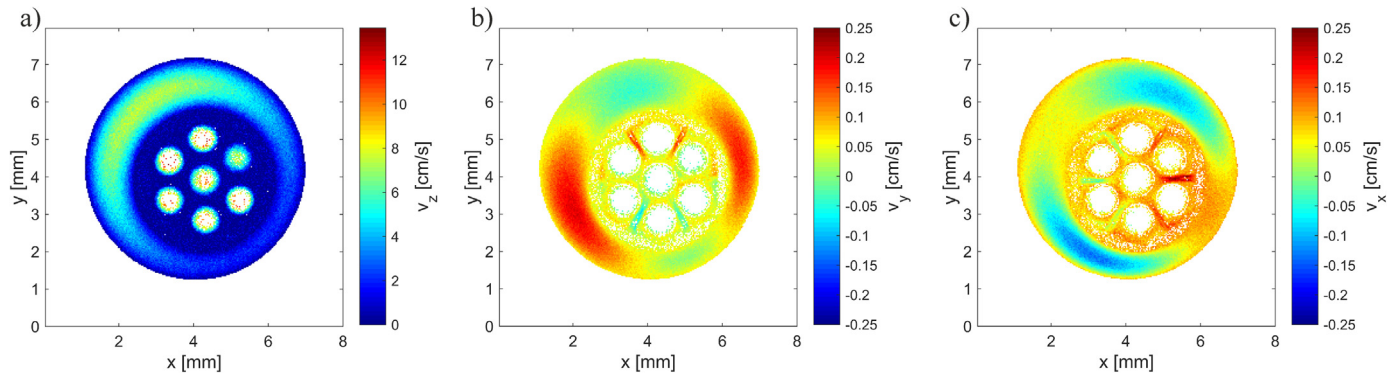


Fig. 6. Velocities in a multichannel hollow fiber module (compare Fig. 1a). (a) v_z along the long axis of the membrane (z -direction in Fig. 1b). (b) v_y transverse in y -direction. (c) v_x transverse in x -direction. As the total flow across the membrane is radially symmetric, the components v_x and v_y show negative and positive values. Note the different scales of the false color bars for v_z and $v_{x,y}$. (For interpretation of the references to color in this figure legend, the reader is referred to the web version of this article).

3.3. Water flow in hollow fiber membrane

An important question in filtration using multichannel membranes concerns the flow distribution. It is unknown in detail how the water flows inside the membrane and how it is distributed into the channels. MRI was used to measure the water flow inside a multichannel membrane in all three directions (x , y and z). To ensure a constant flow over scan time, we used deionized water as feed in these experiments to get an almost constant permeate flux over time. A constant pressure of 0.7 bar was applied.

The highest velocities during “filtration” with deionized water were measured in z direction as expected (Fig. 6a). The velocity in z direction v_z can only be seen in the permeate volume and partly in the seven

feed channels. At too large velocities, signal losses occur due to the outflow of excited ^1H nuclei. The velocities in the channels can therefore only be partially resolved (outflow artifact). Water flow in the membrane pores in the z direction is not visible. When the field of flow (FOF) is set to large values (i.e. 17 cm/s) to measure the velocities in feed channels and permeate volume, the water flow in the supporting material cannot be observed in the images, because the flow resolution is too low to distinguish between zero and very small velocities.

The transverse velocities are approximately a factor of 50 lower compared to the velocities in z direction. Therefore, $\text{FOF}_{x,y}$ was set to the values $v_{y,\text{enc}} = 0.26$ cm/s and $v_{x,\text{enc}} = 0.29$ cm/s which leads to a better resolution for low velocities. Flow in x and y directions was detected in the pores. The flow direction in the pores tends towards the

Table 1
Measurement parameters for the RARE images (Fig. 4(a, b and c), Fig. 5).

MRI parameter	Fig. 4a (deionized water) and Fig. 5	Fig. 4b and c (with GdDTPA)
T_R (T_1 weighting)	2 s	0.5 s
τ_E	10 ms	4.8 ms
$\tau_{E, \text{ieff}}$ (T_2 weighting)	20 ms	4.8 ms
Encoding order	linear	centric
In plane resolution $\Delta x, \Delta y$	29.30 μm	35.16 μm
RARE factor RF	4	2
Number of averages	1	4
Slice thickness	2 mm	2 mm
Scan time	2 min 08 s	4 min 16 s

permeate channel (Fig. 6b and c). Due to the fast flowing ^1H nuclei in the channels (outflow artifact), the signal intensities are too low to determine the velocities in the channels. The same phenomenon was observed in the phase contrast image in the x direction (Fig. 6c) consistent with the y direction. The advective transport in the membrane is evident due to the strong outward transverse direction flows from the center channel localized between the outer channels (Table 1).

3.4. Velocity fields during filtration of aqueous sodium alginate solutions

Sodium alginate ($c_{\text{alginate}} = 200 \text{ mg/L}$) filtrations were performed with a constant pressure of 0.7 bar. The evolution of velocities was measured during filtration in the channels of multichannel hollow fiber membranes, which gives new insights into ultrafiltration processes. The velocities in z direction v_z were measured during filtrations *without* and *with* Ca^{2+} (Fig. 7). Phase contrast images were taken with the pulse sequence shown in Fig. 2. All images were measured with the same

Table 2
Pulse sequence parameters used in the flow map sequence, i.e. measurement of velocities.

MRI parameter	Fig. 6	Fig. 7
T_R	2 s	0.2 s
τ_E	6.2 ms	4.6 ms
In plane resolution $\Delta x, \Delta y$	31.25 μm	31.25 μm
Slice thickness	2 mm	2 mm
Number of averages	2	4
Scan time	34 min 08 s	6 min 49 s

parameters (Table 2) except for v_{enc} , because of the change in velocity during filtration ($v_{\text{enc}} \in [1, 20] \text{ cm/s}$). As expected, the velocity component in the z direction was the largest and showed the biggest change during filtration. The volume flow in the channels \dot{V}_{Channel} could be calculated from the phase contrast images by summing up the velocities in each channel and multiplying them by the pixel resolution in x and y direction ($\Delta x * \Delta y$). Here, the assumption was made that velocities in x and y direction are very small (Fig. 6b and c) and can be neglected in the volumetric flow calculation.

$$\dot{V}_{\text{Channel}} \approx \dot{V}_{z, \text{Channel}} = \sum v_{z,i} * (\Delta x * \Delta y). \quad (4)$$

Hence the change in volumetric flow with fouling under constant pressure was measured.

In the filtration *without* Ca^{2+} , v_z decreases in the channels during filtration time due to fouling (Fig. 7a, b and c) in accordance with the observation of deposit formation. After 34 min the channels seem to be completely filled by the alginate concentration polarization layer, and flow in the z direction has nearly ceased. The velocities in the permeate channel also decrease, but not as strongly as in the channels. This

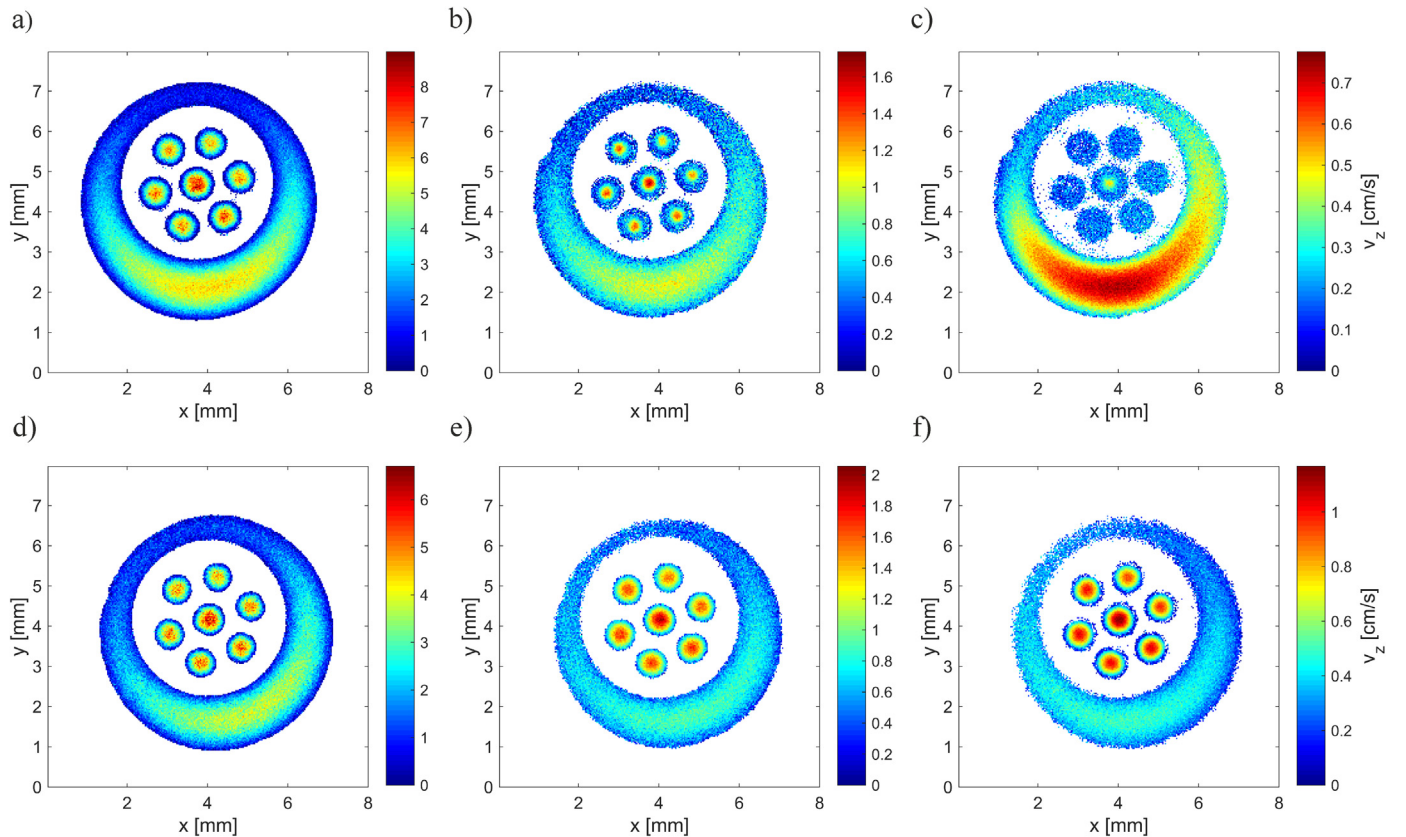


Fig. 7. Velocity images during a filtration of alginate ($c_{\text{alginate}} = 200 \text{ mg/L}$) *without* Ca^{2+} (with increasing filtration time from left to right): (a) "Filtration" with deionized water. (b) After 11 min of filtration and (c) after 34 min of filtration *without* Ca^{2+} ($c_{\text{Ca}^{2+}} = 2 \text{ mmol/L}$) (d) "Filtration" of deionized water before starting the filtration *with* Ca^{2+} : (e) After 11 min of filtration and (f) after 34 min of filtration *with* Ca^{2+} . Please note the different scales of the false color bars which encode v_z .

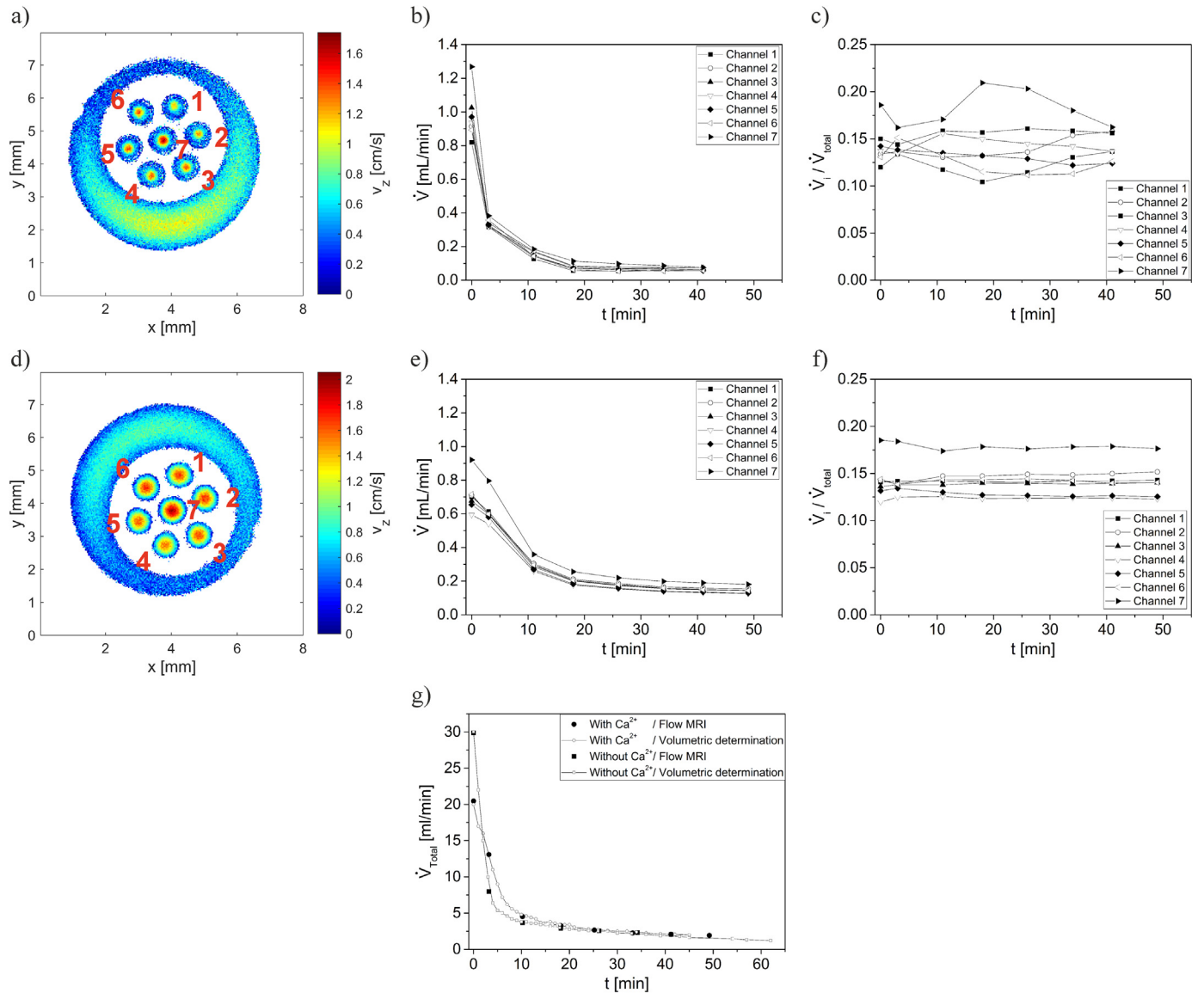


Fig. 8. Quantification of volume flow (see Eq. (4)) in channels: Velocity images at 11 min with the assignment of the channels for the experiment (a) *without* Ca^{2+} and (d) *with* Ca^{2+} . (b) Absolute volume flow as a function of filtration time t in the filtration *without* Ca^{2+} and (e) *with* Ca^{2+} . (c) $\dot{V}_i / \dot{V}_{\text{total}}$ of each channel for the filtration *without* Ca^{2+} and (f) *with* Ca^{2+} . (g) Comparison of the volume flow volumetrically measured with the volume flow measured by MRI. The consistency of the data proves the overall agreement of the macroscopic filtration and the microscopic MRI views. The lines are guides to the eye.

suggests that the alginate is flushed to the end of the module and concentrates first at the end and subsequently towards the inlet of the module. This phenomenon means that the ratio between the velocities in the membrane and the velocities in the permeate change during filtration time. With increasing filtration time, the main filtration will be increasingly restricted towards the inlet of the module. These observations are consistent with previous findings where the deposit formation during filtration of an aqueous solution of sodium alginate *without* Ca^{2+} was a function of z , and the thickest fouling layer is observed at the end of the module [18].

Fouling was different in the filtration *with* Ca^{2+} due to the formation of a gel (Fig. 7d, e and f). The velocities in z direction were also decreasing, but compared to the filtration *without* Ca^{2+} the channels do not seem to be completely blocked in agreement with the geometry of the deposit in the structural images. A finite velocity $v_z > 0$ was measured in all channels after a filtration time of 34 min. This indicates that the gel layer is not easily flushed to the end of module by shear forces of the feed flow in the channels. The gel layer adheres to the membrane's surface, generating a more uniform fouling layer along z . This

observation is in good agreement with previous work, where the deposit layer in the filtration of alginate *with* Ca^{2+} depends not as strongly on z as in the filtration of alginate *without* Ca^{2+} [18].

An important question concerns the flow distribution in the channels of a multichannel membrane: How is the distribution and how does it change with filtration time? MRI is capable to measure the velocity field spatially resolved, thus the volume flow in each channel can be calculated. Thus the spatial heterogeneity of the transport processes during filtration can be quantified. The volume flow of each channel is a function of filtration time (Fig. 8b and e) comparable to previous findings [17]. A difference at the beginning of the filtration depending on the Ca^{2+} concentration was observed: The volume flow of the filtration *without* Ca^{2+} was larger than in the filtration *with* Ca^{2+} . This can be explained by the fact that in this experiment the membrane was used first for the filtration *without* Ca^{2+} , was afterwards cleaned by flushing the deposits out of the membrane lumen with deionized water. Some small amounts of the deposit could be left on the membrane's surface, so that the volume flow at the beginning of the second filtration was lower. To quantify the flow in the individual channels during filtration,

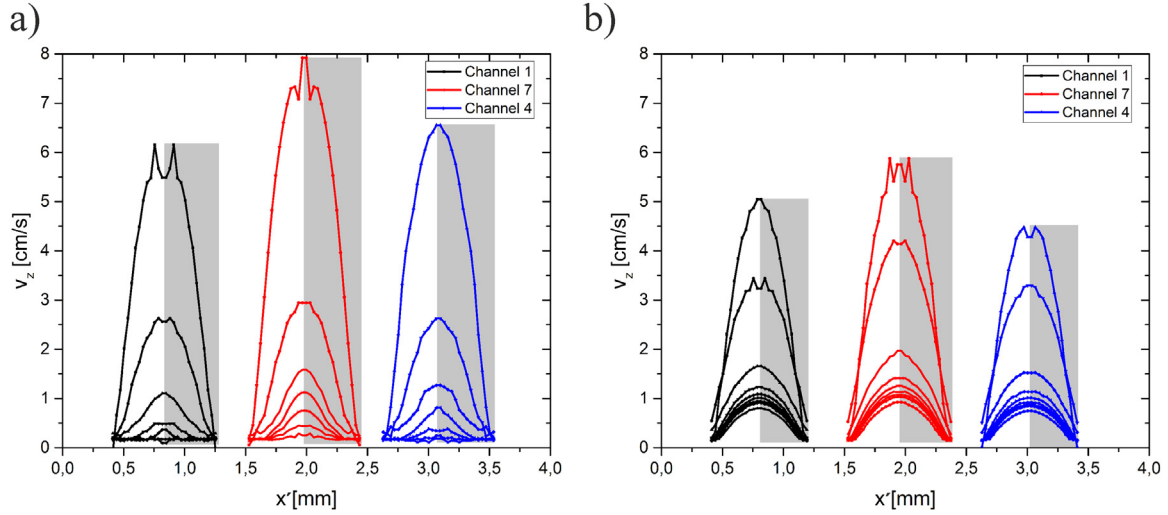


Fig. 9. MRI velocity profiles for the filtration (a) *without* Ca^{2+} and (b) *with* Ca^{2+} . x' denotes a spatial coordinate which connects the three channels but differs from the x -axis in the images. The profiles have partially a gray background, these points were mirrored from the left profile, because the ring analysis gives just a radial dependence. For both filtrations the velocities decrease during the filtration time.

the volume flow was normalized to the total volume flow: $\dot{V}_i / \dot{V}_{total}$. *Without* Ca^{2+} the highest ratio is in the center channel 7 over the whole filtration. Noticeably, some fluctuations were observed during filtration in all channels. This hints at small flow irregularities during filtration. A potential source of these fluctuations are alginate molecules or clusters which cannot withstand the shear forces of the feed solution and are flushed towards the end of the membrane, while others stick better on the membrane surface. *With* Ca^{2+} the ratio for all channels 1-7 are approximately constant over the filtration time. Again, the center channel 7 shows the highest ratio. The proportionalities of the channel ratios during the filtration stay almost constant when compared to the filtration *without* Ca^{2+} , where the ratios change. This can be explained by the fact that alginate *with* Ca^{2+} forms a gel layer, i.e. a more uniform fouling layer with higher adhesion to the membrane. This leads to a more constant proportionality.

The channels filtrate almost evenly except of the center channel 7 in both filtrations. Notably channel 7 of the membrane exhibits the highest velocities and the highest volume flow in z direction. This is probably due to the flow conditions at the inlet of the membrane: The module is connected to a tube with an inner diameter of 4 mm and a length of 1.50 m. Flow in this tube is described by a Hagen Poiseuille flow profile. The membrane has an outer diameter of 4 mm, and the channels have a diameter of 0.9 mm. The highest velocity in the center of the 4 mm tube is probably due to the Poiseuille profile may result in a higher entrance velocity in the channel in the center of the membrane. This interpretation has to be confirmed by further experiments.

3.4.1. Flow profiles in membrane channels from phase contrast images

Flow profiles, i.e. velocity distributions, were analyzed. In previous work a ring method was implemented to analyze the deposit layers in a membrane lumen from MR intensity images [18]. This method was transferred to calculate flow profiles in each channel from velocity images: An ellipse is created at the edge of the channel in a velocity image. The mean velocity of voxel elements in this ellipse is calculated, and afterwards the next ellipse is created one pixel inwards, towards the center of the channel. Naturally, the number of averaged pixels decreases toward the center leading to an increase of statistical errors. Consequently, spikes in Fig. 9 appear predominantly in the center of the feed channels. This allows calculation of the radial velocity profiles from the surface towards the feed center in each of the seven channels. Due to the mirroring described in Fig. 9 these fluctuations are over emphasized.

Velocity profiles were calculated for the filtration *without* and *with*

Ca^{2+} in channel 1, 7 and 4 (Fig. 8a and d) to see the difference between the center channel and the external channels (Fig. 9). The flow profiles are different for both filtrations. *With* Ca^{2+} a Poiseuille profile is observed during the complete filtration. A compact gel layer builds up, which causes an increase of filtration resistance and consequently lower velocities. For the filtration *without* Ca^{2+} , flow profiles are biased to higher velocity towards the center of the channel and deviate more and more from the Poiseuille profile along the filtration process. This phenomenon is caused by the build up of a concentration polarization layer. The viscosity increases near the inner surface of the channels due to the accumulation of alginate molecules. Instead of building up a compact gel layer (*with* Ca^{2+}), a concentration polarization layer builds up, which changes the flow profile.

4. Conclusions

Intensity images from μCT and MRI measurements can show the structure of inner pores of polymer hollow fiber membranes. Air trapping inside the membrane and their change due to diffusive and convective transport over time can be observed and quantified by MRI.

Sodium alginate was used as model substance causing fouling during filtration. CaCl_2 allows the realization of different filtration mechanisms. Concentration polarization and a gel layer fouling was observed also in the multichannel membranes. The contrast agent MagAlg90 improves the image contrast between feed solution and fouling layer, which allows characterization of the deposit in multi channel polymeric membranes. Results show that the center channel is not as strongly fouled as the outer channels in the filtration *without* Ca^{2+} . The channels for the filtration *with* Ca^{2+} were filtrated more uniformly due to the different fouling mechanism.

Velocity fields were measured by phase contrast MRI. The ratio of the single channel volume flow and the total volume flow was used to quantify the filtration performance in each of the seven channels. The outer channels perform evenly except for the channel in the center. Here, the velocities and volume flows are slightly higher. This effect can be observed in both types of filtration. The small difference between the center channel and the surrounding channels remains over the complete filtration time. The ratios between the surrounding channels only slightly change during. *Without* Ca^{2+} the ratio fluctuates more than for the filtration *with* Ca^{2+} , which is attributed to the different filtration mechanisms.

Flow profiles could be extracted by a mean ring method of radial mean velocities. The flow profile during the filtration *without* Ca^{2+}

changes to a more acute flow profile towards the center of the channel lumen attributed to viscosity changes. For the filtration *with* Ca^{2+} , the flow is describable by a Poiseuille flow profile over the complete filtration. The identification of the different mechanisms in each channel could help in optimization of these multichannel membranes and of the conditions in which they are operated. Further investigations of the backwash behavior along the hollow fiber membrane (z direction) will be carried out in order to better understand the ultrafiltration process in these polymeric multichannel membranes.

Acknowledgements

The authors thank the German Research Foundation (DFG) for financial support of the instrumental facility Pro²NMR, the MRI CFD project (GU1123/5 1) as well as of the update of the MRI console. Furthermore we would like to thank the Karlsruhe House of Young Scientists (KHYS) for funding for the stay at Montana State University (MSU) in U.S.A. JDS and SLC thank the U.S. NSF MRI program and the M.J. Murdock Charitable Trust for equipment funding.

References

- [1] Inge GmbH, Selected UF References, 2018. <<http://www.inge.basf.com/ev/internet/inge/de/function/conversions/publish/content/inge/Referenzen/Reference List.pdf>> (Accessed 20 April 2018).
- [2] T. Melin, R. Rautenbach, Membranverfahren: Grundlagen der Modul- und Anlagenauslegung, Springer Berlin Heidelberg, Heidelberg, 2013.
- [3] A.K. Pabby, S.S.H. Rizvi, A.M.S. Requena, Handbook of Membrane Separations: Chemical, Pharmaceutical, Food, and Biotechnological Applications, Taylor & Francis, Boca Raton, 2008.
- [4] M. Heijnen, R. Winkler, P. Berg, Optimisation of the geometry of a polymeric Multibore® ultrafiltration membrane and its operational advantages over standard single bore fibres, *Desalin. Water Treat.* 42 (2012) 24–29.
- [5] S. Bütehorn, L. Utiu, M. Küppers, B. Blümich, T. Wintgens, M. Wessling, T. Melin, NMR imaging of local cumulative permeate flux and local cake growth in submerged microfiltration processes, *J. Membr. Sci.* 371 (2011) 52–64.
- [6] P.Z. Culfaz, Microstructured Hollow Fibers and Microsieves: Fabrication, Characterization and Filtration Applications, University of Twente, Enschede, 2010.
- [7] D. Airey, S. Yao, J. Wu, V. Chen, A.G. Fane, J.M. Pope, An investigation of concentration polarization phenomena in membrane filtration of colloidal silica suspensions by NMR micro-imaging, *J. Membr. Sci.* 145 (1998) 145–158.
- [8] S.A. Creber, J.S. Vrouwenvelder, M.C.M. van Loosdrecht, M.L. Johns, Chemical cleaning of biofouling in reverse osmosis membranes evaluated using magnetic resonance imaging, *J. Membr. Sci.* 362 (2010) 202–210.
- [9] R.V. Linares, L. Fortunato, N.M. Farhat, S.S. Bucs, M. Staal, E.O. Fridjonsson, M.L. Johns, J.S. Vrouwenvelder, T. Leiknes, Mini-review: novel non-destructive in situ biofilm characterization techniques in membrane systems, *Desalin. Water Treat.* 57 (2016) 22894–22901.
- [10] E.O. Fridjonsson, S.J. Vogt, J.S. Vrouwenvelder, M.L. Johns, Early non-destructive biofouling detection in spiral wound RO membranes using a mobile earth's field NMR, *J. Membr. Sci.* 489 (2015) 227–236.
- [11] X. Yang, E.O. Fridjonsson, M.L. Johns, R. Wang, A.G. Fane, A non-invasive study of flow dynamics in membrane distillation hollow fiber modules using low-field nuclear magnetic resonance imaging (MRI), *J. Membr. Sci.* 451 (2014) 46–54.
- [12] S.A. Creber, T.R.R. Pintelon, D.A. Graf von der Schulenburg, J.S. Vrouwenvelder, M.C.M. van Loosdrecht, M.L. Johns, Magnetic resonance imaging and 3D simulation studies of biofilm accumulation and cleaning on reverse osmosis membranes, *Food Bioprod. Process.* 88 (2010) 401–408.
- [13] J.S. Vrouwenvelder, D.A. Graf von der Schulenburg, J.C. Kruithof, M.L. Johns, M.C.M. van Loosdrecht, Biofouling of spiral-wound nanofiltration and reverse osmosis membranes: a feed spacer problem, *Water Res.* 43 (2009) 583–594.
- [14] D.A. Graf von der Schulenburg, J.S. Vrouwenvelder, S.A. Creber, M.C.M. van Loosdrecht, M.L. Johns, Nuclear magnetic resonance microscopy studies of membrane biofouling, *J. Membr. Sci.* 323 (2008) 37–44.
- [15] C.A. Heath, G. Belfort, B.E. Hammer, S.D. Mirer, J.M. Pimbley, Magnetic resonance imaging and modeling of flow in hollow-fiber bioreactors, *AIChE J.* 36 (1990) 547–558.
- [16] B.E. Hammer, C.A. Heath, S.D. Mirer, G. Belfort, Quantitative flow measurements in bioreactors by nuclear magnetic resonance imaging, *Nat. Biotechnol.* 8 (1990) 327.
- [17] F. Arndt, S. Schuhmann, G. Guthausen, S. Schütz, H. Nirschl, In situ MRI of alginate fouling and flow in ceramic hollow fiber membranes, *J. Membr. Sci.* 524 (2017) 691–699.
- [18] S. Schuhmann, N. Schork, K. Beller, H. Nirschl, T. Oerther, G. Guthausen, In-situ characterization of deposits in ceramic hollow fiber membranes by compressed sensing RARE-MRI, *AIChE J.* 64 (2018).
- [19] N. Schork, S. Schuhmann, F. Arndt, S. Schütz, G. Guthausen, H. Nirschl, MRI investigations of filtration: fouling and cleaning processes, *Micro. Mesopor. Mat.* 269 (2018) 60–64.
- [20] F. Arndt, U. Roth, H. Nirschl, S. Schütz, G. Guthausen, New Insights into Sodium Alginate Fouling of Ceramic Hollow Fiber Membranes by NMR Imaging, *AIChE J.* 62 (2016) 2459–2467.
- [21] H.D. Park, I.S. Chang, K.J. Lee, Principles of Membrane Bioreactors for Wastewater Treatment, (2015).
- [22] K. Katsoufidou, S.G. Yiantisios, A.J. Karabelas, An experimental study of UF membrane fouling by humic acid and sodium alginate solutions: the effect of backwashing on flux recovery, *Desalination* 220 (2008) 214–227.
- [23] K. Listiari, W. Chun, D.D. Sun, J.O. Leckie, Fouling mechanism and resistance analyses of systems containing sodium alginate, calcium, alum and their combination in dead-end fouling of nanofiltration membranes, *J. Membr. Sci.* 344 (2009) 244–251.
- [24] K. Listiari, L.H. Tan, D.D. Sun, J.O. Leckie, Systematic study on calcium-alginate interaction in a hybrid coagulation-nanofiltration system, *J. Membr. Sci.* 370 (2011) 109–115.
- [25] P. Mi, H. Cabral, D. Kokuryo, M. Rafi, Y. Tereda, I. Aoki, T. Saga, I. Takehiko, N. Nishiyama, K. Kataoka, Gd-DTPA-loaded polymere metal complex micelles with high relaxivity for MR cancer imaging, *Biomaterials* 34 (2013) 492–500.
- [26] Inge GmbH, Inge Operator's manual 2.1, in, 2014.
- [27] R.V. Mulkern, S.T.S. Wong, C. Winalski, F.A. Jolesz, Contrast manipulation and artifact assessment of 2d and 3d RARE sequences, *Magn. Reson. Imaging* 8 (1990) 557–566.
- [28] G.A. Webb, Annual Reports on NMR Spectroscopy, 1st ed., Academic Press, 2017.
- [29] R. Kimmich, NMR - Tomography Diffusometry Relaxometry, Springer Verlag, Berlin, 1997.
- [30] P.T. Callaghan, Principles of Nuclear Magnetic Resonance Microscopy, Oxford University Press, New York, 1991.
- [31] B. Blümich, NMR Imaging of Materials, Clarendon Press; Oxford University Press, Oxford; New York, 2000.

Repository KITopen

Dies ist ein Postprint/begutachtetes Manuskript.

Empfohlene Zitierung:

Schuhmann, S.; Simkins, J.; Schork, N.; Codd, S.; Seymour, J.; Heijnen, M.; Saravia, F.; Horn, H.; Nirschl, H.; Guthausen, G.

[Characterization and quantification of structure and flow in multichannel polymer membranes by MRI.](#)

2018. Journal of membrane science, 570-571

[doi: 10.5445/IR/1000088460](#)

Zitierung der Originalveröffentlichung:

Schuhmann, S.; Simkins, J.; Schork, N.; Codd, S.; Seymour, J.; Heijnen, M.; Saravia, F.; Horn, H.; Nirschl, H.; Guthausen, G.

[Characterization and quantification of structure and flow in multichannel polymer membranes by MRI.](#)

2018. Journal of membrane science, 570-571, 472–480.

[doi:10.1016/j.memsci.2018.10.072](#)

Lizenzinformationen: [KITopen-Lizenz](#)